Title of the project	Enhanced safety materials for Li-ion batteries
Short title	ENSAMAT
TRL:	1-3
Code:	09I04-03-V02-00028
Beginning of the project:	1.1.2025
Duration:	20 months

Deliverable number	**Deliverable**	**Work package code**	**Entity responsible for deliverable**	**Type**	**Access and dissemination**	**Method of verification**	**Delivery (project implementation month)**
D4.3	**Ageing behaviour and safet operational limits of selected batteries**	WP4	STU	Report	P	Experimentálne výsledky	M20

Obsah

1. Introduction 3

2. Temperature-dependent electrochemical performance and model-based evaluation of operation limits during charging 5

3. Aging of SiG based batteries 10

3.1 Cycling aging behaviour of SiG based in different SOC window 10

3.2 Impact of OCV Evolution during aging on SOC Estimation Accuracy 14

4. Analysis of lithium plating/stripping under low-temperature charging conditions 17

5. Summary of the obtained results 21

1. Introduction

Within Work Package 4, this activity focused on investigating the ageing behaviour and operational limits of commercially available lithium-ion batteries with silicon–graphite (SiG) composite anodes. The objective was to generate experimental data and validated modelling tools that improve the understanding of battery behaviour under different operating conditions, identify the mechanisms governing degradation and safety, and support the definition of safe operating boundaries for advanced lithium-ion battery systems.

Commercial SiG lithium-ion cells were intentionally selected as representative and well-characterised model systems for studying electrochemical behaviour, ageing mechanisms and charging limitations before transferring the developed methodologies to advanced battery materials investigated within the ENSAMAT project. The obtained knowledge therefore provides a methodological basis for the future evaluation of next-generation electrode materials and safety-enhancing technologies developed by the project partners.

The report is organised into three complementary technical sections that together address battery performance, degradation and operational safety.

Chapter 2 investigates the temperature-dependent electrochemical performance and model-based evaluation of charging operation limits. Temperature-dependent quasi-open-circuit voltage (quasi-OCV) characterisation, Hybrid Pulse Power Characterisation (HPPC), and equivalent circuit modelling are combined to establish a validated electrochemical model of the battery. The developed model is subsequently employed to evaluate and compare multiple fast-charging strategies under different ambient temperatures, allowing the identification of charging protocols that provide the most favourable compromise between charging speed and thermal loading.

Chapter 3 focuses on the ageing behaviour of silicon-enriched graphite batteries. The influence of different state-of-charge operating windows on degradation mechanisms is investigated using capacity fade analysis, pseudo-open-circuit voltage (pseudo-OCV) measurements, incremental capacity analysis (ICA), and electrochemical impedance spectroscopy (EIS). Particular attention is devoted to degradation of the silicon component, its influence on pseudo-OCV evolution, and the resulting impact on state-of-charge estimation accuracy throughout battery ageing.

Chapter 4 investigates the occurrence of lithium plating and stripping during low-temperature charging, one of the most critical degradation and safety mechanisms in high-energy lithium-ion batteries. Experimental measurements combining relaxation voltage analysis and electrochemical impedance spectroscopy are employed to identify electrochemical signatures associated with lithium plating and stripping. The obtained results provide the

basis for future in-operando diagnostic methodologies capable of early detection of hazardous charging conditions and support the development of safer fast-charging strategies.

Overall, the results presented in this deliverable provide complementary knowledge on the temperature-dependent performance, degradation behaviour and operational limits of silicon–graphite lithium-ion batteries. The developed experimental methodologies, diagnostic approaches and modelling tools contribute to a deeper understanding of degradation mechanisms relevant to advanced lithium-ion batteries and support the future development of safer battery systems, improved battery management strategies, and the evaluation of novel battery materials developed within the ENSAMAT project.

2. Temperature-dependent electrochemical performance and model-based evaluation of operation limits during charging

The commercial Molicel INR21700-P50B was selected for characterisation and modeling. This cylindrical cell combines a silicon enriched graphite anode with a NCA cathode. The silicon enriched anode distinguishes it from conventional graphite only cells and determines its electrochemical behaviour discussed below.

Quasi-open-circuit voltage (quasi-OCV) measurements were performed at C/20 from −40 °C to 50 °C in 10 °C steps to determine equilibrium electrochemical properties. Both charge and discharge directions were measured at each temperature. Figure 2.1 shows the OCV-SOC-temperature curves.

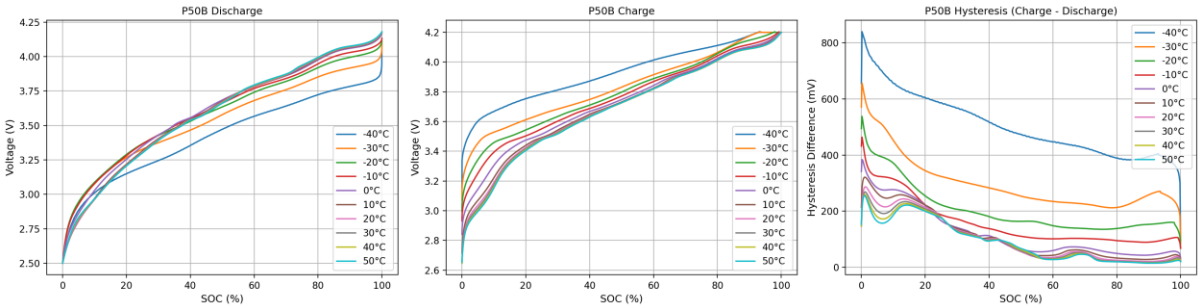


Figure 2. 1: C/20 discharge (left), charge (centre), and OCV hysteresis (right) curves of the Molicel INR21700-P50B cell measured at temperatures from −40 °C to 50 °C

Both discharge and charge OCV profiles show strong temperature dependence, with the largest at low SOC. Below 0 °C the discharge voltage curves shift down due to increased internal impedance and reduced electrode accessibility. The graphite lithiation plateau remains visible across all temperatures. The P50B cell exhibits unusually large OCV hysteresis. It exceeds 600 mV at low SOC and temperature, and remains between 100-200 mV at mid-SOC even at room temperature.

The usable discharge capacity was determined from C/20 discharge measurements across the full temperature range. Results are shown in Figure 2.2.

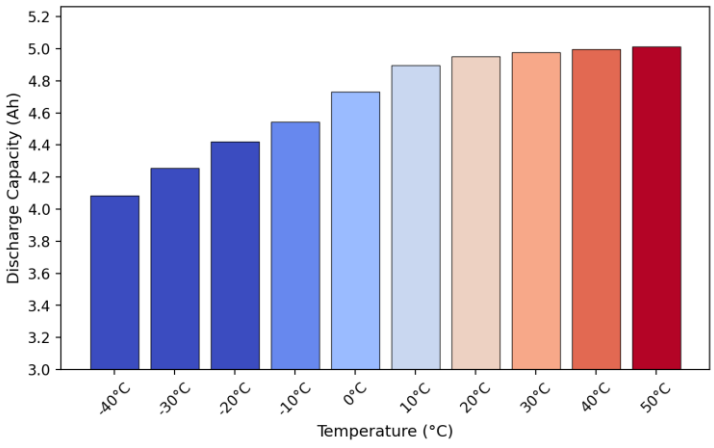


Figure 2. 2: Discharge capacity of the Molicel INR21700-P50B cell as a function of temperature from −40 °C to 50 °C, measured at C/20

At 50 °C, capacity reaches 5.01 Ah, matching the nominal rating. Capacity decreases linearly with temperature. The decline is gradual above 0 °C but steepens below, consistent with slowing lithium-ion diffusion in the electrolyte and electrode materials. The total capacity loss from 50 °C to -40 °C is 18%. The SiG anode is more sensitive to low temperature than graphite. As silicon diffusivity declines more steeply below 0 °C, and two-phase lithiation becomes increasingly kinetically limited.

HPPC measurements were performed to characterise dynamic electrical behaviour and develop a model for simulation and battery management. The dataset includes -20 °C to 50 °C in 10 °C steps. At -30 °C and -40 °C, pulsed-current voltage response became too large so these measurements were excluded from the model. Measurements cover SOC points across 0-100% in both charge and discharge directions. Each HPPC pulse consists of current steps at defined amplitudes followed by relaxation periods to extract ohmic resistance and transient response. The data was used to parameterise a equivalent circuit model (ECM) shown in Figure 2.3.

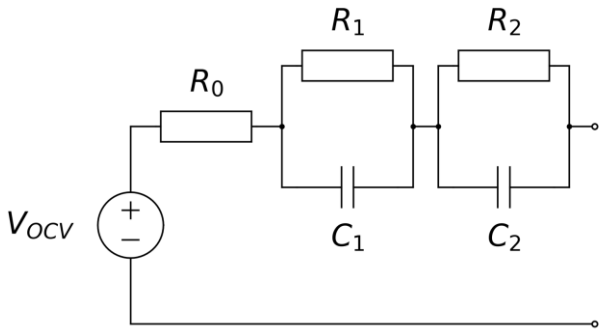


Figure 2. 3: Second-order equivalent circuit model (2-RC ECM) used for the Molicel INR21700-P50B cell

It comprises an open-circuit voltage source (quasi-OCV), ohmic resistance R_o for electrolyte and contact losses, and two RC branches: R_1C_1 for fast transients and R_2C_2 for slow relaxation. This structure is standard for battery simulation and state estimation, balancing complexity with the accuracy achievable from HPPC measurements.

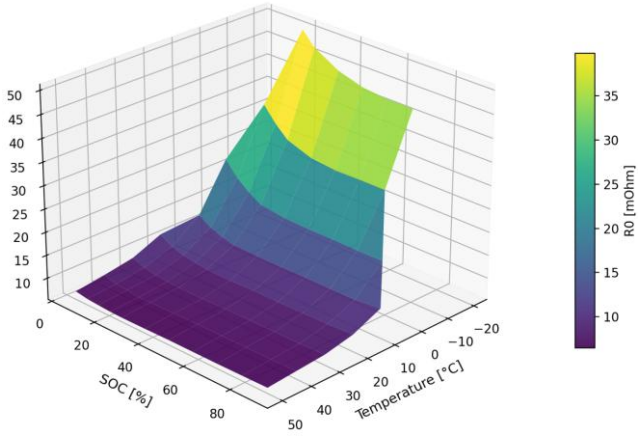


Figure 2.4: Ohmic resistance R_o of the Molicel INR21700-P50B cell as a function of temperature and SOC from HPPC charge-side measurements

Figure 2.4 shows the temperature and SOC dependence of ohmic resistance R_0 extracted from HPPC data. R_0 increases with decreasing temperature, reflecting reduced ionic conductivity in the liquid electrolyte at low temperatures. SOC dependence is weak at room temperature but becomes pronounced at sub-zero temperatures. The low-temperature increase in R_0 is a primary factor limiting power delivery and fast charging in cold conditions and shapes the charging protocols discussed below. The parameterised ECM was validated against independent dynamic current profiles. The model showed good agreement with measured terminal voltage across the operating range, as can be seen in Figure 2.5.

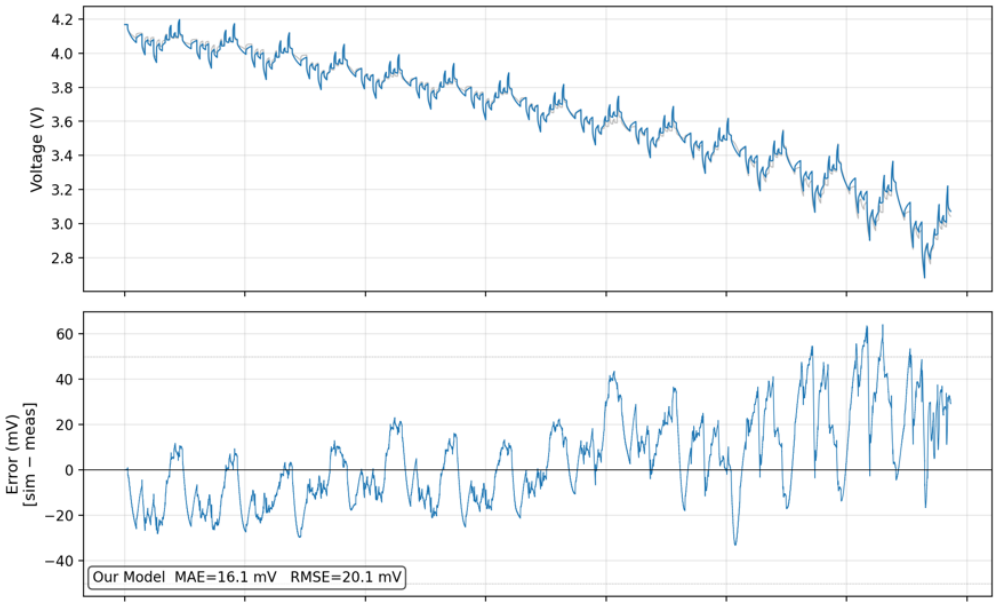


Figure 2. 5: 2RC P50B ECM model verification

The validated temperature-dependent ECM was used to benchmark charging operation protocols across the speed–thermal trade-off space. Five protocol families were considered: constant current (CC), constant current–constant voltage (CC-CV), multistage constant current (MSCC), pulse charging, and sigmoid current ramps.

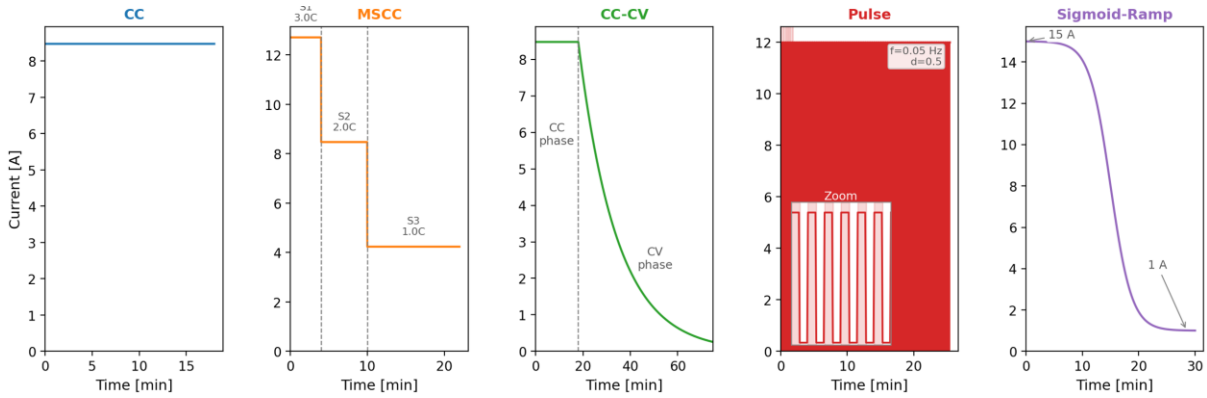


Figure 2.6: Benchmarked protocol families

103 protocol variants were simulated at six ambient temperatures (−10 °C to 40 °C), for a total of 618 simulations. All protocols were evaluated over the 20–80 % SOC range for fast charging.

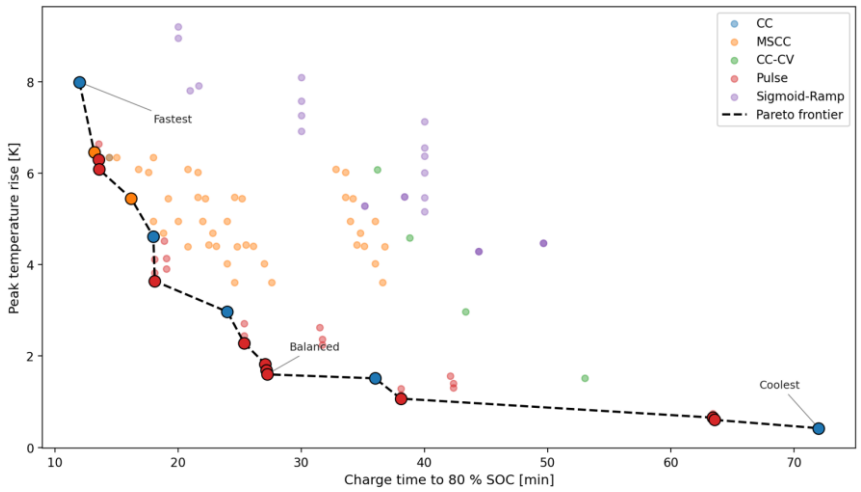


Figure 2.7: Speed–thermal trade-off scatter of 103 charging protocols at 20 °C

The Pareto frontier is composed almost entirely of pulse charging protocols, with a few CC and MSCC variants. CC-CV and sigmoid ramps do not appear, because the CV taper in CC-CV adds charge time without proportional heating reduction, and sigmoid ramps front-load current, heating the cell before the slow tail can compensate. For any given charge-time target, pulse charging achieves lower thermal stress than any other tested protocol family. This ranking holds across all ambient temperatures, as shown in Figure 2.7. The relative ordering of protocol families does not change - pulse charging consistently performs best at every temperature.

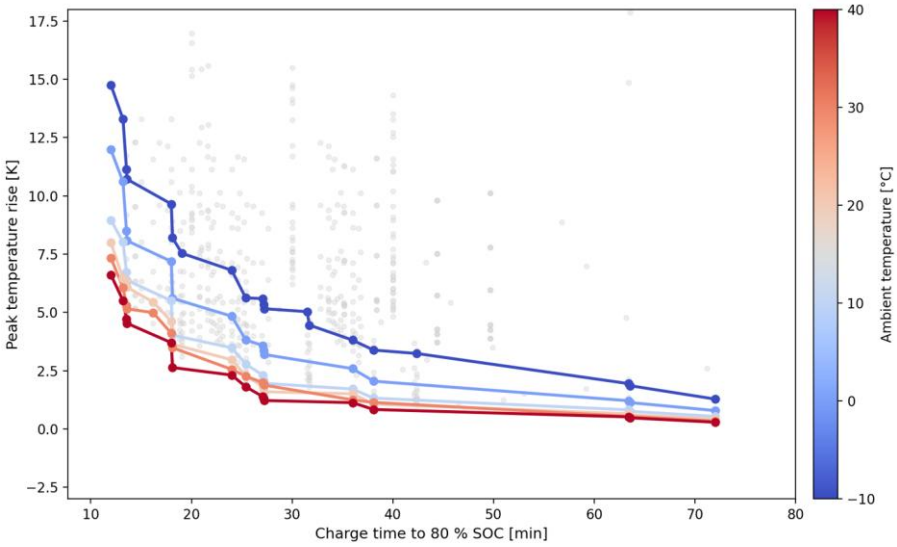


Figure 2.8: Temperature-dependent shift of the Pareto frontier across six ambient temperatures from −10 °C to 40 °C

Conclusion

The presented electrochemical characterisation established a comprehensive temperature-dependent dataset describing the behaviour of the commercial Molicel INR21700-P50B silicon-enriched lithium-ion cell. The results confirmed that low temperatures significantly influence the equilibrium voltage characteristics, increase OCV hysteresis, reduce available capacity, and substantially increase internal resistance, thereby limiting charging performance and increasing thermal stress. These findings highlight the necessity of incorporating temperature-dependent electrochemical properties into battery models used for charging control.

The parameterised and experimentally validated second-order equivalent circuit model provided a reliable representation of the cell behaviour over a wide operating temperature range and enabled systematic evaluation of charging operation limits. Simulation of 103 charging protocol variants demonstrated that the trade-off between charging speed and thermal loading strongly depends on ambient temperature. Among the investigated strategies, pulse charging consistently achieved the most favourable speed–thermal compromise across all evaluated temperatures, outperforming conventional CC, CC–CV, multistage CC and sigmoid charging approaches.

Overall, this work demonstrates that combining temperature-dependent electrochemical characterisation with validated battery modelling provides an effective methodology for defining safe and efficient charging operating limits. The developed approach offers a practical framework for optimisation of fast-charging strategies and can support the development of advanced battery management systems for next-generation silicon-enriched lithium-ion batteries.

3. Aging of SiG based batteries

3.1 Cycling aging behaviour of SiG based in different SOC window

The aim of this work was to investigate how SOC-window-dependent degradation of Li-ion batteries with Gr/SiOx (SiG) anodes influences the evolution of pseudo-OCV profiles and how these changes translate into SOC estimation errors. Silicon degradation was selectively induced or suppressed using low-, high-, and full-SOC cycling regimes, while electrical and electrochemical characterisation based on capacity fade analysis, incremental capacity analysis and electrochemical impedance spectroscopy was used to support the interpretation of the observed degradation behaviour.

Methodology

Commercial 18650 cells, Molicel M35A, were used in this study. The anode of these cells consists of approximately 87 wt% graphite, 10 wt% SiOx and 3 wt% inactive components. The cathode is based on lithium nickel–cobalt–aluminium oxide. The nominal capacity of the cells is 3.5 Ah, with charge and discharge voltage limits of 4.2 V and 2.5 V, respectively. All cycling experiments were performed in a temperature-controlled laboratory at 25 °C.

Three distinct operating regimes were designed to selectively induce or suppress silicon-related degradation. The low-SOC regime consisted of CC charging to 3.7 V and CC discharging to 2.5 V (Figure 3.1a). The high-SOC regime involved CCCV charging to 4.2 V and CC discharging to 3.8 V (Figure 3.1b). The full-SOC regime followed the full charge–discharge voltage window between 4.2 V and 2.5 V (Figure 3.1c). Charging/discharging current corresponded to 1C.

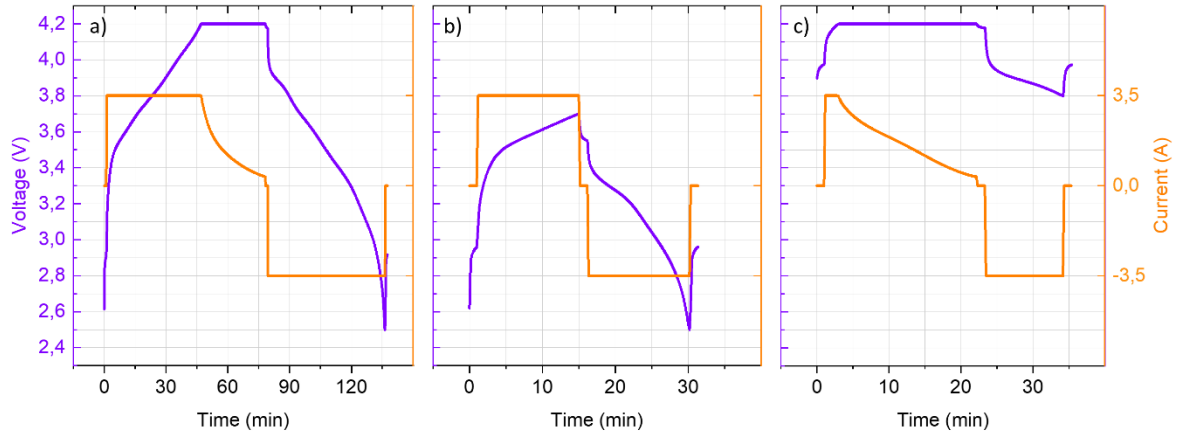


Figure 3.1: Voltage and current settings for a) low-SOC regime, b) high-SOC regime, and for c) full-SOC regime.

The experimental work was divided into two measurement sets. In the first set, 15 cells were cycled, with five cells were assigned to each operating regime. This part of the experiment was used to analyse the degradation behaviour associated with individual SOC operating windows. The characterisation step included full charge–discharge cycles, a slow C/20 cycle used to obtain pseudo-OCV profiles, and EIS measurements on selected cells. In the second measurement set, four fresh cells were cycled under semi-randomised cycling scenarios. Each

scenario consisted of 500-cycle blocks composed of different proportions of low-SOC, high-SOC and full-SOC cycles. These scenarios were designed to represent more heterogeneous cycling histories.

Degradation Behaviour under Different SOC Operating Windows

The capacity fade analysis clearly demonstrated that cycling within distinct SOC regimes resulted in significantly different degradation rates (Figure 3.2). High-SOC cycling led to relatively stable capacity retention, indicating that degradation of the silicon component was largely suppressed under this regime. In contrast, full-SOC cycling resulted in a more pronounced but still relatively gradual capacity decline. Low-SOC cycling followed a nearly identical capacity trend as the full-SOC scenario up to ~250 equivalent full cycles, after which, cells cycled within the low-SOC regime exhibit accelerated degradation, with SOH dropping to ~60% after only ~350 equivalent full cycles. This accelerated degradation under low-SOC operation is consistent with the expected behaviour of Gr/SiOx anodes. Low-SOC cycling promotes deeper delithiation of the anode and stronger utilisation of the silicon component, which can lead to mechanical stress, particle cracking, electrical isolation and continuous SEI growth. These processes reduce the reversible capacity contribution of silicon and contribute to loss of lithium inventory.

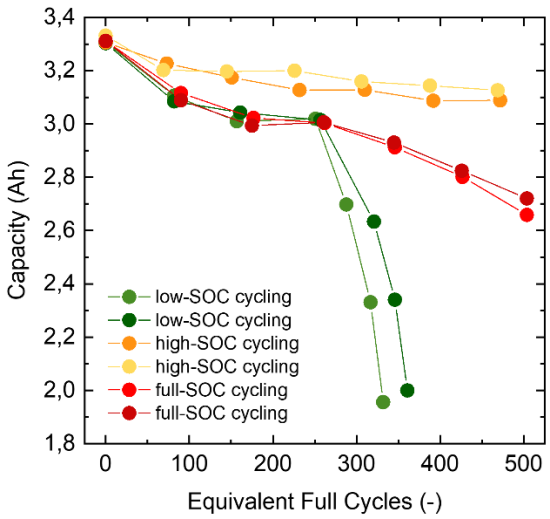


Figure 3.2: Development of discharge capacities for cells cycled within individual low-, full-, and high-SOC cyclic scenarios.

The evolution of pseudo-OCV profiles (Figure 3.3a-b) further confirmed that the OCV–SOC relationship is not invariant during ageing. Cells cycled under the high-SOC regime showed strong overlap of pseudo-OCV profiles, suggesting relatively stable electrochemical behaviour. In the full-SOC regime, the pseudo-OCV profiles gradually shifted towards higher voltages. The most pronounced pseudo-OCV evolution was observed for cells cycled under the low-SOC regime, where the voltage profiles changed significantly with ageing. These observations show that the degradation-induced evolution of the pseudo-OCV profile depends strongly on the SOC operating window. Since the shape of the OCV profile reflects the relative contribution of

graphite and silicon, the observed changes are consistent with progressive degradation of the silicon component in the Gr/SiOx anode.

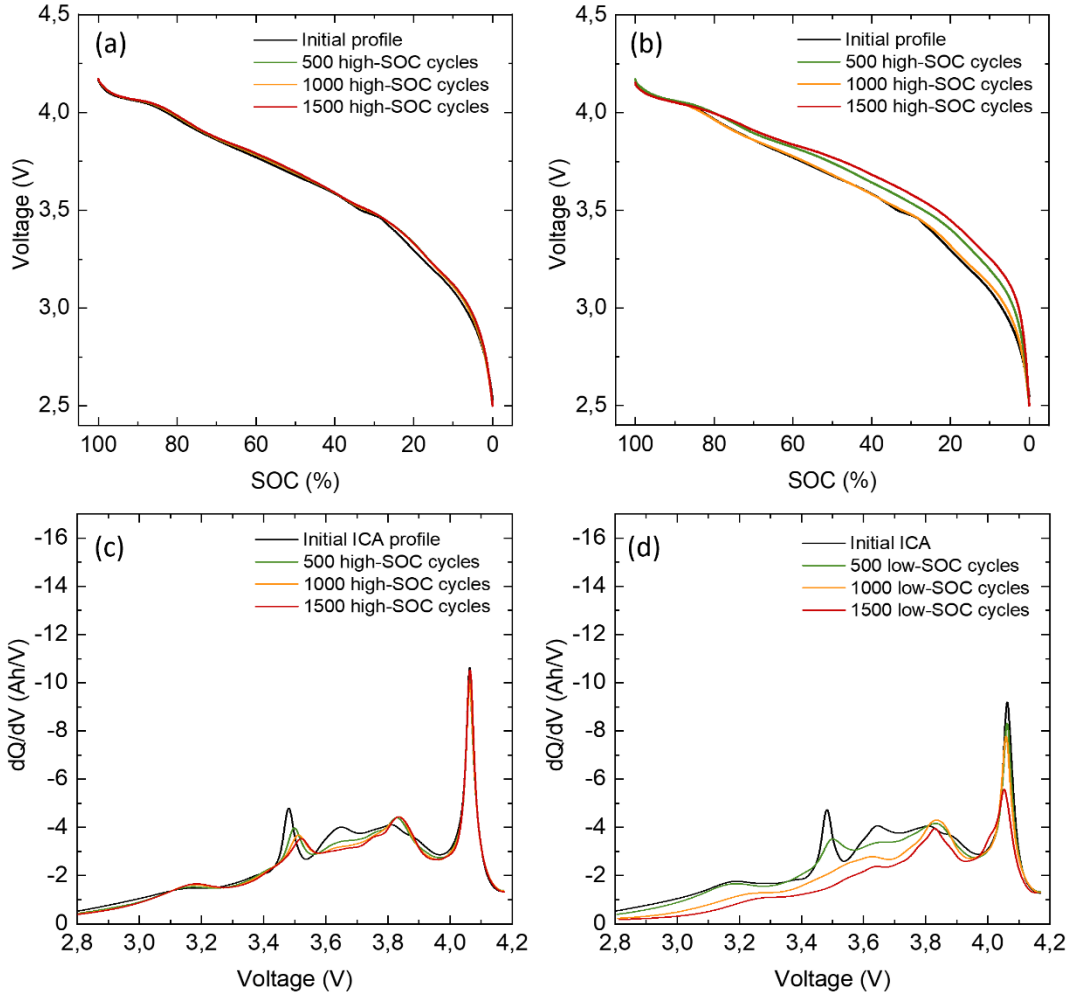


Figure 3. 3: Evolution of pseudo-OCV profiles for a) high- and b) low-SOC cyclic scenarios; corresponding ICA profiles for c) high- and d) low-SOC cycling scenario.

Incremental capacity analysis (Figure 3.3c-d) provided further support for this interpretation. Under high-SOC cycling, the main ICA features remained relatively stable after the initial cycles, suggesting that both the Gr/SiOx negative electrode and the NCA positive electrode remained electrochemically stable. Under full-SOC cycling, more pronounced changes appeared in the ICA curves, including a decrease in the silicon-related feature. These changes indicate progressive loss of active silicon. The most significant changes were observed under low-SOC cycling. The silicon-related ICA feature showed a pronounced decrease in magnitude and a shift towards higher voltages, while the feature associated with loss of lithium inventory also decreased. This behaviour clearly reflects progressive loss of active silicon and is consistent with the accelerated capacity fade observed under low-SOC operation. Since degradation of the silicon component contributes to lithium loss through particle isolation and repeated SEI growth, silicon degradation can be considered a dominant source of degradation in this regime.

EIS measurements confirmed the degradation pathways observed from the capacity and ICA analyses. Under high-SOC cycling (Figure 3.4), the fitted impedance parameters remained stable throughout the experiment. Under full-SOC cycling, the most notable change was an increase in the charge-transfer resistance, consistent with progressive loss of active material. Under low-SOC cycling, the changes were much more pronounced. The SEI resistance practically doubled, the charge-transfer resistance increased substantially, and the diffusion-related response decreased significantly. These results are consistent with mechanical degradation and pulverisation of the silicon component, leading to increased SEI growth, loss of active material and impaired ion transport.

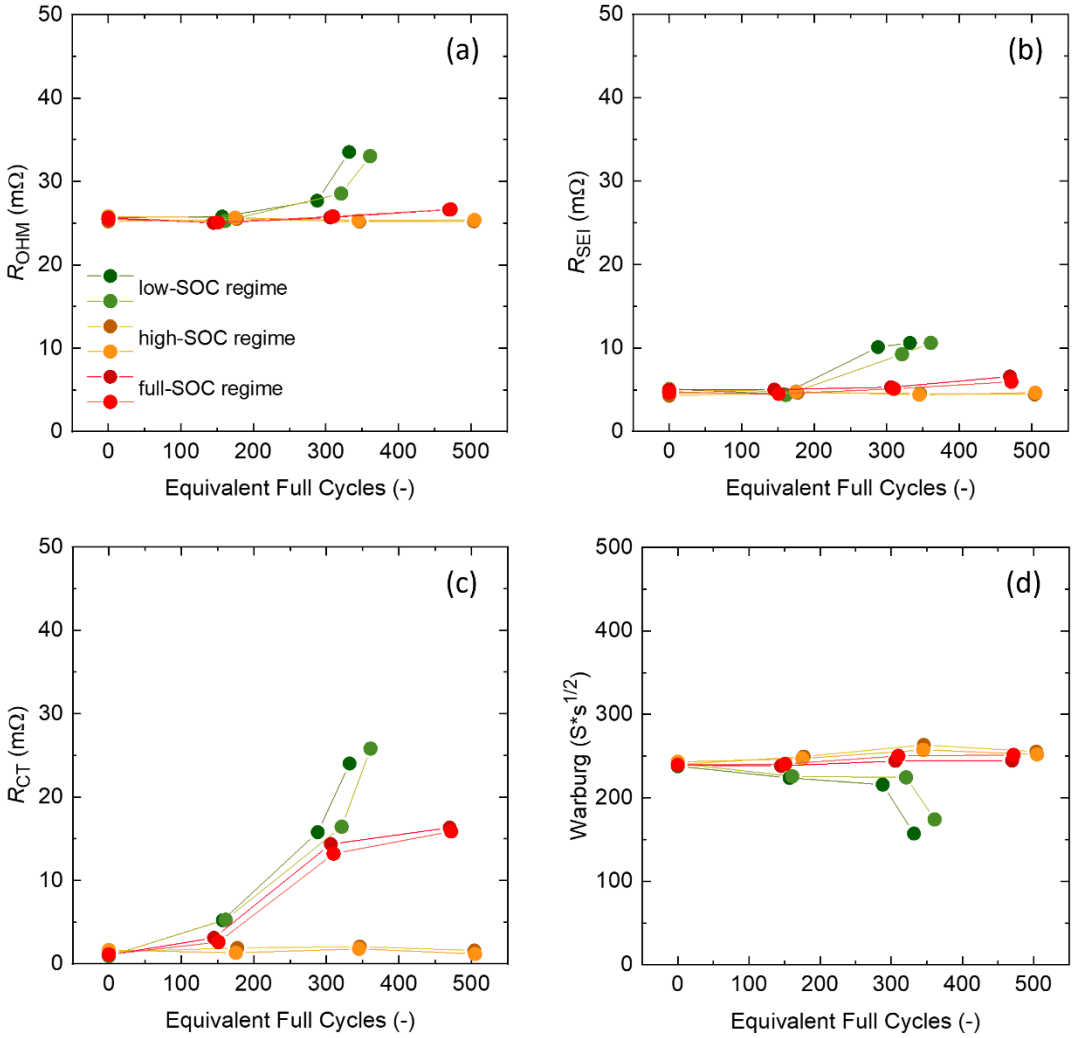


Figure 3.4: Results of the EIS data fitting: (a) R_{OHM}, (b) R_{SEI}, (c) R_{CT}, and (d) Warburg element.

Overall, the electrical and electrochemical characterisation demonstrates that cells cycled under high-SOC, full-SOC and low-SOC regimes follow distinct degradation pathways. In particular, low-SOC cycling induces accelerated degradation of the silicon component in the Gr/SiOx anode. This degradation has a significant influence on the evolution of the pseudo-OCV profile, highlighting the strong relationship between degradation mechanisms and OCV behaviour.

3.2 Impact of OCV Evolution during aging on SOC Estimation Accuracy

The second part of the study focused on the practical consequence of degradation-induced pseudo-OCV evolution for SOC estimation. Since many SOC estimation methods rely on the OCV–SOC relationship, changes in the pseudo-OCV profile during ageing can introduce systematic SOC estimation errors (Figure 3.5a-b).

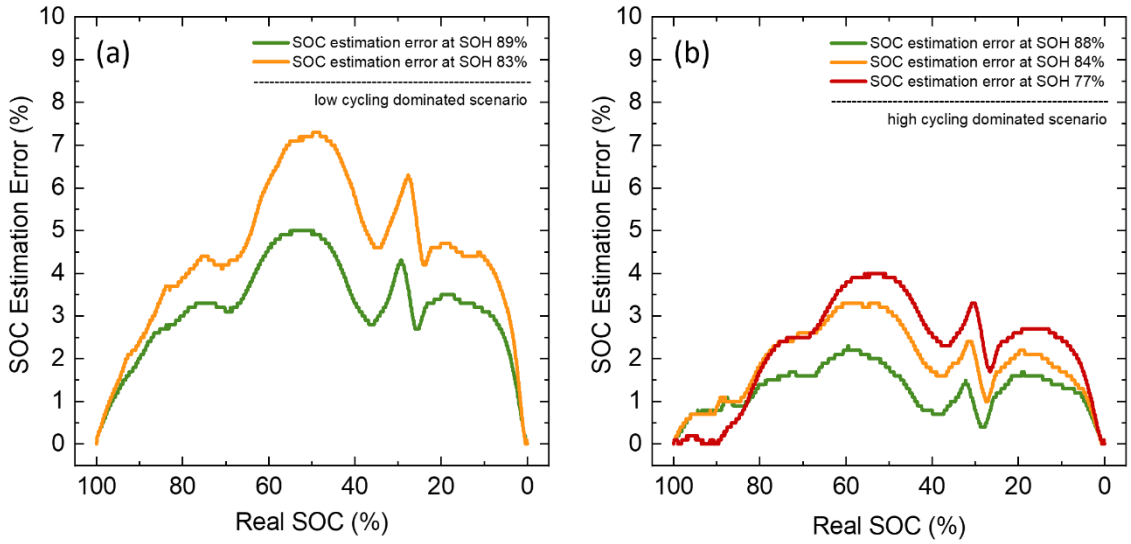


Figure 3.5: SOC estimation error as a function of real SOC levels for a) low-SOC cycling dominated, and b) high-SOC cycling dominated scenario.

Pseudo-OCV profiles obtained from the semi-randomised cycling scenarios showed a progressive deviation from the initial OCV profile in all measured cells. However, the magnitude of this deviation depended strongly on the cycling history. At comparable SOH levels of approximately 83%, the high-SOC-dominated scenario exhibited the lowest OCV drift, while full-SOC- and low-SOC-dominated scenarios showed substantially larger deviations. The largest OCV drift was observed for the low-SOC-dominated scenario, supporting the conclusion that silicon-related degradation strongly affects the evolution of the OCV–SOC relationship. This result is important because it shows that cells with comparable remaining capacity may exhibit significantly different pseudo-OCV profiles depending on their cycling history. Therefore, SOH assessment based only on capacity retention does not fully describe the electrochemical state of Li-ion batteries with Gr/SiOx anodes. Two cells may have similar SOH values but different OCV–SOC relationships due to different silicon-related degradation pathways

To quantify the impact on SOC estimation, the initial pseudo-OCV profile was used as a reference OCV–SOC mapping. Voltage values from degraded pseudo-OCV profiles were projected onto this initial mapping, and the resulting absolute SOC estimation errors were evaluated. This approach represents a situation where the original OCV–SOC relationship is used despite degradation-induced changes in the cell voltage profile. The results showed that degradation-induced pseudo-OCV evolution can lead to substantial SOC estimation errors. For the full-SOC-dominated scenario, the mean absolute SOC estimation error approached 4%

near the conventional end-of-life criterion. For the low-SOC-dominated scenario, the error was slightly higher at comparable SOH and local errors exceeded 7% in the mid-SOC region. The most severe case was observed in the strongly low-SOC-dominated scenario at advanced degradation, where the mean absolute SOC estimation error reached approximately 6% and local errors approached 8–9%. In contrast, the high-SOC-dominated scenario showed considerably lower SOC estimation errors. Even at a comparable SOH level, the error was approximately half of that observed for the low-SOC-dominated case. This demonstrates that the SOC estimation error is not governed solely by the remaining capacity of the cell, but also by the degradation pathway through which the cell reached that capacity.

The key finding is that Li-ion batteries with Gr/SiOx anodes may develop different OCV–SOC relationships even when they exhibit comparable SOH levels. Low-SOC-dominated cycling leads to stronger silicon degradation, more pronounced pseudo-OCV drift and consequently higher SOC estimation errors. High-SOC-dominated cycling, on the other hand, results in more stable pseudo-OCV behaviour and lower SOC estimation error. These findings highlight a limitation of conventional SOH-based approaches for correcting OCV–SOC maps. For Gr/SiOx anodes, it may not be sufficient to update the OCV–SOC relationship only as a function of capacity fade. Instead, cycling history and phase-selective degradation of silicon should also be considered, particularly for ageing-aware SOC estimation frameworks and second-life battery applications.

Conclusion

This work investigated the influence of SOC-window-dependent degradation on the evolution of pseudo-OCV profiles and the resulting SOC estimation errors in commercial Li-ion batteries with Gr/SiOx composite anodes. The results demonstrate that different SOC operating windows lead to distinct degradation pathways. High-SOC cycling resulted in relatively stable electrochemical behaviour, while full-SOC cycling caused more noticeable degradation. The most severe degradation was observed under low-SOC cycling, where accelerated loss of active silicon, increased impedance and pronounced pseudo-OCV evolution were identified. The study also showed that capacity retention alone does not fully describe the electrochemical state of Li-ion batteries with Gr/SiOx anodes. Cells with similar SOH may exhibit markedly different OCV–SOC relationships depending on their cycling history. This behaviour directly affects the accuracy of OCV-based SOC estimation. When the initial OCV–SOC relationship was used as a reference for degraded cells, substantial SOC estimation errors were observed. These errors were highest for low-SOC-dominated cycling histories and lowest for high-SOC-dominated histories. At comparable SOH levels, the SOC estimation error for the low-SOC-dominated scenario was approximately twice as high as that observed for the high-SOC-dominated scenario. At advanced degradation levels relevant for second-life applications, the error became even more pronounced.

Overall, the results show that cycling-history-dependent, phase-selective degradation of silicon should be considered when developing SOC estimation approaches for Li-ion batteries

with Gr/SiOx anodes. Future ageing-aware SOC estimation methods should account not only for capacity fade, but also for the degradation-induced evolution of the OCV–SOC relationship throughout battery lifetime.

4. Analysis of lithium plating/stripping under low-temperature charging conditions

In this part of the work, commercially available Molicel P50B lithium-ion cells with silicon–graphite composite anodes were investigated with the aim of identifying electrochemical signatures related to lithium plating/stripping under low-temperature charging conditions. The cells were charged using a pulsed protocol at a current corresponding to 0.5C, followed by relaxation periods. The measurements were performed at four different temperatures: +15 °C, 0 °C, −15 °C and −30 °C (Figure 4.1).

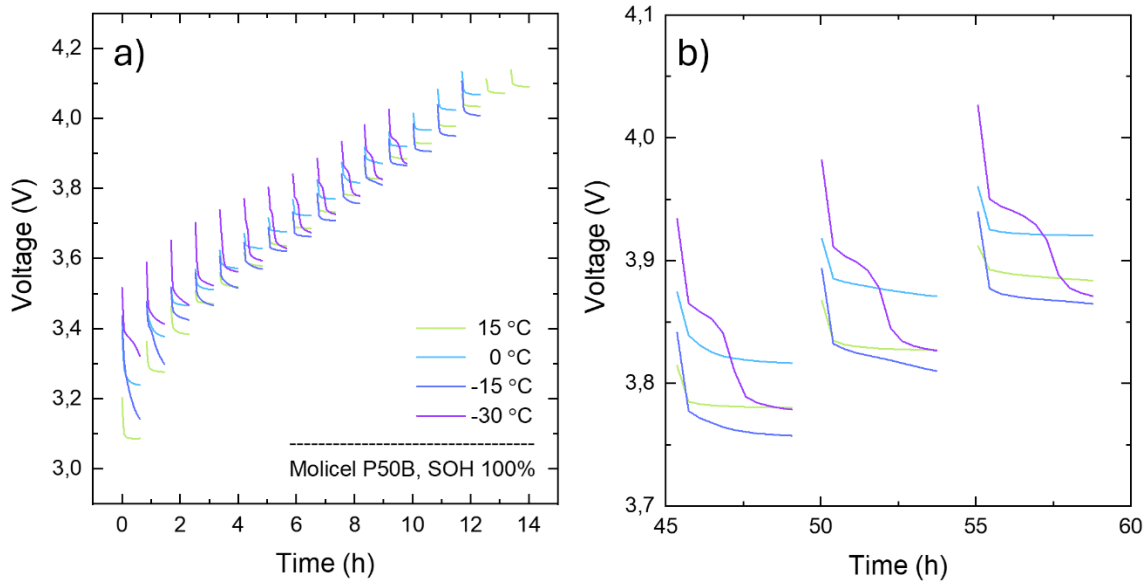


Figure 4. 1. a) Relaxation voltages after charging periods; b) close-up

To enhance the visibility of such features, the relaxation voltage profiles were numerically differentiated. The resulting derivative profiles are shown in Figure 4.2a–d for +15 °C, 0 °C, −15 °C and −30 °C, respectively. At higher temperatures, no clear feature attributable to lithium stripping was observed. However, at −30 °C, a distinct peak appeared in the derivative profile, which can be assigned to lithium stripping during the relaxation period. In addition, the onset of this feature shifted towards longer relaxation times with an increasing number of measurements, suggesting a gradual evolution of the plating/stripping behaviour under repeated low-temperature charging.

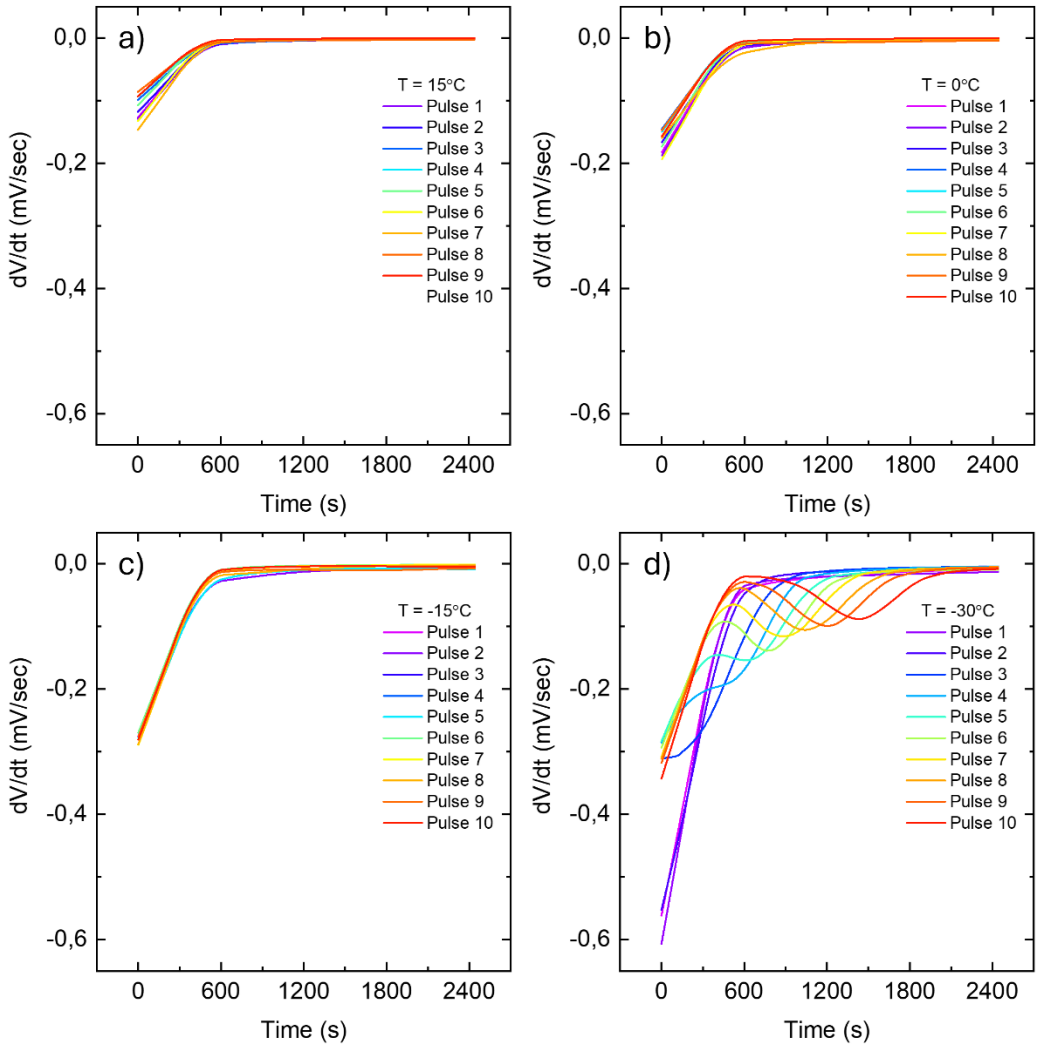


Figure 4.2: Derivations of relaxation profiles, where a) represents measurements at 15°C, b) 0°C, d) -15°C, and d) at -30°C.

In the next step, the relationship between the relaxation voltage profile and the impedance response was evaluated. The changes in the real, imaginary and complex impedance magnitude were analysed as a function of frequency and compared with the corresponding relaxation voltage profiles. Pearson correlation coefficients and standard deviations were calculated for individual frequencies, and the results are summarised in Table 1. This analysis provides an initial indication of which EIS frequencies are most sensitive to changes associated with lithium stripping.

Table 1. Pearson correlation parameters

T (°C)	f (Hz)	r - Z real vs f	r - Z imag vs f	r - Z abs vs f	std - Z real vs f	std - Z imag vs f	std - Z abs vs f
15°C	4973,32	-0,76	0,97	0,83	0,33	0,02	0,14
	2801,07	-0,93	0,97	-0,48	0,04	0,02	0,48
	1582,03	-0,95	0,96	-0,94	0,02	0,02	0,03
	885,42	-0,96	0,96	-0,96	0,02	0,02	0,02
	502,23	-0,97	0,96	-0,97	0,02	0,01	0,02
	282,38	-0,96	0,96	-0,96	0,02	0,02	0,02
	158,01	-0,97	0,97	-0,97	0,02	0,01	0,02
	89,29	-0,96	0,96	-0,96	0,01	0,01	0,01
	49,87	-0,96	0,96	-0,96	0,01	0,01	0,01
	27,90	-0,96	0,96	-0,96	0,01	0,01	0,01
	15,63	-0,97	0,96	-0,97	0,01	0,01	0,01
	8,88	-0,96	0,96	-0,96	0,02	0,01	0,02
	5,01	-0,96	0,96	-0,96	0,02	0,02	0,02
	2,82	-0,95	0,90	-0,95	0,02	0,06	0,02
	1,58	-0,95	0,92	-0,95	0,02	0,05	0,02
	0,89	-0,93	0,86	-0,93	0,03	0,09	0,03
	0,50	-0,90	0,79	-0,90	0,04	0,16	0,04
	0,28	-0,84	0,81	-0,84	0,08	0,18	0,07
	0,16	-0,71	0,86	-0,74	0,17	0,17	0,15
	0,09	-0,50	0,78	-0,56	0,44	0,45	0,40
a)	0,05	-0,28	0,80	-0,42	0,60	0,46	0,54
	0,03	-0,03	0,70	-0,30	0,71	0,59	0,61

T (°C)	f (Hz)	r - Z real vs f	r - Z imag vs f	r - Z abs vs f	std - Z real vs f	std - Z imag vs f	std - Z abs vs f
0°C	4973,32	-0,92	0,98	-0,35	0,11	0,01	0,74
	2801,07	-0,95	0,99	-0,86	0,05	0,01	0,22
	1582,03	-0,97	0,99	-0,97	0,03	0,01	0,03
	885,42	-0,98	0,99	-0,98	0,02	0,01	0,02
	502,23	-0,98	0,99	-0,98	0,02	0,01	0,01
	282,38	-0,99	0,99	-0,99	0,01	0,01	0,01
	158,01	-0,99	0,99	-0,99	0,01	0,01	0,01
	89,29	-0,98	0,98	-0,99	0,01	0,01	0,01
	49,87	-0,99	0,98	-0,99	0,01	0,01	0,01
	27,90	-0,99	0,98	-0,98	0,01	0,01	0,01
	15,63	-0,98	0,98	-0,98	0,01	0,01	0,01
	8,88	-0,98	0,98	-0,98	0,01	0,01	0,01
	5,01	-0,98	0,98	-0,98	0,01	0,02	0,01
	2,82	-0,98	0,98	-0,98	0,01	0,02	0,01
	1,58	-0,98	0,99	-0,98	0,01	0,01	0,01
	0,89	-0,98	0,98	-0,98	0,01	0,01	0,01
	0,50	-0,98	0,97	-0,98	0,01	0,02	0,01
	0,28	-0,98	0,97	-0,98	0,01	0,02	0,01
	0,16	-0,98	0,97	-0,98	0,01	0,04	0,01
	0,09	-0,99	0,94	-0,99	0,01	0,13	0,01
b)	0,05	-0,98	0,86	-0,98	0,01	0,41	0,01
	0,03	-0,97	0,83	-0,97	0,02	0,48	0,02

T (°C)	f (Hz)	r - Z real vs f	r - Z imag vs f	r - Z abs vs f	std - Z real vs f	std - Z imag vs f	std - Z abs vs f
-15°C	4973,32	-0,88	0,98	-0,84	0,33	0,03	0,44
	2801,07	-0,92	0,98	-0,88	0,22	0,02	0,34
	1582,03	-0,95	0,98	-0,96	0,08	0,03	0,07
	885,42	-0,96	0,98	-0,97	0,04	0,03	0,03
	502,23	-0,97	0,98	-0,98	0,03	0,02	0,03
	282,38	-0,98	0,98	-0,98	0,03	0,02	0,03
	158,01	-0,98	0,98	-0,98	0,03	0,02	0,03
	89,29	-0,97	0,98	-0,98	0,03	0,02	0,02
	49,87	-0,97	0,98	-0,98	0,03	0,02	0,02
	27,90	-0,97	0,98	-0,98	0,03	0,02	0,02
	15,63	-0,97	0,98	-0,98	0,04	0,02	0,02
	8,88	-0,97	0,98	-0,98	0,04	0,01	0,02
	5,01	-0,98	0,98	-0,98	0,03	0,01	0,02
	2,82	-0,98	0,98	-0,98	0,02	0,01	0,01
	1,58	-0,98	0,98	-0,98	0,01	0,01	0,01
	0,89	-0,98	0,99	-0,98	0,01	0,01	0,01
	0,50	-0,98	0,99	-0,98	0,01	0,01	0,01
	0,28	-0,99	0,99	-0,99	0,01	0,01	0,01
	0,16	-0,99	0,99	-0,99	0,01	0,01	0,01
	0,09	-0,98	0,98	-0,98	0,02	0,02	0,01
c)	0,05	-0,98	0,98	-0,98	0,02	0,02	0,02
	0,03	-0,98	0,97	-0,98	0,02	0,03	0,02

T (°C)	f (Hz)	r - Z real vs f	r - Z imag vs f	r - Z abs vs f	std - Z real vs f	std - Z imag vs f	std - Z abs vs f
-30°C	4973,32	-0,98	0,97	-0,97	0,02	0,03	0,02
	2801,07	-0,98	0,98	-0,98	0,02	0,02	0,02
	1582,03	-0,98	0,98	-0,98	0,02	0,02	0,02
	885,42	-0,98	0,98	-0,98	0,02	0,02	0,02
	502,23	-0,98	0,98	-0,98	0,02	0,02	0,02
	282,38	-0,98	0,98	-0,98	0,02	0,02	0,02
	158,01	-0,98	0,98	-0,98	0,02	0,02	0,02
	89,29	-0,98	0,98	-0,98	0,02	0,02	0,02
	49,87	-0,97	0,98	-0,98	0,02	0,02	0,02
	27,90	-0,97	0,98	-0,98	0,02	0,02	0,02
	15,63	-0,96	0,98	-0,98	0,03	0,02	0,02
	8,88	-0,94	0,98	-0,98	0,03	0,02	0,02
	5,01	-0,91	0,98	-0,98	0,06	0,02	0,02
	2,82	-0,95	0,98	-0,98	0,07	0,02	0,03
	1,58	-0,97	0,98	-0,98	0,05	0,02	0,03
	0,89	-0,98	0,98	-0,98	0,04	0,02	0,03
	0,50	-0,98	0,98	-0,98	0,03	0,02	0,03
	0,28	-0,98	0,99	-0,98	0,03	0,01	0,03
	0,16	-0,98	0,99	-0,98	0,03	0,01	0,03
	0,09	-0,98	0,99	-0,98	0,03	0,01	0,03
d)	0,05	-0,98	0,98	-0,98	0,03	0,02	0,03
	0,03	-0,98	0,83	-0,98	0,02	0,54	0,02

The broader aim of this experiment is to identify suitable frequency regions for future dynamic EIS measurements that could be integrated directly into the charging protocol. Such an approach would enable the in-operando detection of lithium plating and stripping during charging, rather than only during subsequent relaxation. These experiments therefore represent an initial screening step towards the development of more advanced diagnostic methods for detecting lithium plating in silicon–graphite based lithium-ion cells.

The use of Molicel P50B cells with silicon–graphite composite anodes is particularly relevant, as this type of anode may be more prone to lithium plating under specific operating conditions, especially during low-temperature charging. Since lithium plating is one of the critical degradation and safety-related mechanisms in high-energy lithium-ion batteries, reliable methods for its detection are of significant importance. In future work, the present methodology will be extended by implementing dynamic EIS during charging and by combining the electrochemical measurements with complementary diagnostic techniques, including calorimetry, acoustic defectoscopy and strain measurements.

5. Summary of the obtained results

This report presents the results of experimental and modelling activities carried out within Work Package 4 to investigate the ageing behaviour and safety operational limits of commercially available lithium-ion batteries with silicon–graphite composite anodes. The work combines electrochemical characterisation, battery modelling and advanced diagnostic methodologies to improve the understanding of battery performance, degradation mechanisms and safety-related phenomena under different operating conditions. Together, the presented studies provide complementary knowledge supporting the development of safer battery systems and advanced battery management strategies.

The temperature-dependent electrochemical characterisation and equivalent circuit modelling demonstrated the strong influence of temperature on battery performance and charging capability. The developed model enabled the comparison of multiple charging strategies over a broad operating range and identified pulse charging as the most favourable approach for minimising thermal stress while maintaining fast charging performance. These results establish a quantitative basis for defining safe operational limits and optimising charging protocols for silicon-enriched graphite batteries.

The ageing investigations demonstrated that degradation behaviour is strongly dependent on the selected state-of-charge operating window. Low-SOC cycling accelerated silicon-related degradation, leading to increased impedance growth, pronounced evolution of pseudo-open-circuit voltage profiles and significantly higher state-of-charge estimation errors. In contrast, high-SOC cycling resulted in considerably more stable electrochemical behaviour. These findings show that batteries with similar State-of-Health may follow fundamentally different degradation pathways and that capacity retention alone is insufficient to fully describe the ageing state of silicon-containing lithium-ion batteries.

The study of lithium plating under low-temperature charging further demonstrated the capability of electrochemical techniques to identify early signatures of safety-critical degradation mechanisms. Relaxation voltage analysis combined with electrochemical impedance spectroscopy provided valuable insight into the onset of lithium plating and identified promising frequency regions for future dynamic impedance measurements during charging. The presented methodology therefore establishes an important basis for future in-operando diagnostics capable of detecting hazardous operating conditions before irreversible degradation or safety incidents occur.

Overall, the results demonstrate that battery ageing and operational safety are governed by a combination of electrochemical, thermal and kinetic processes that cannot be fully understood using conventional electrical measurements alone. The complementary experimental methodologies and modelling approaches presented in this deliverable provide a comprehensive framework for analysing battery behaviour, defining safe operational limits and improving battery state estimation throughout battery lifetime.

The methodologies and knowledge developed within this activity establish a scientific and methodological foundation for subsequent work within the ENSAMAT project. In particular, they provide validated experimental procedures and modelling tools that can be directly applied to the advanced battery materials and safety-enhancing technologies developed by the project partners, thereby supporting the development of safer, more reliable and longer-lasting next-generation lithium-ion batteries.

Although the three studies address different aspects of battery behaviour, they consistently demonstrate that electrochemical performance, ageing mechanisms and safety limitations are strongly interconnected and therefore require a combined experimental and modelling approach.